



Cite this: *Chem. Commun.*, 2023, 59, 12346

Received 19th June 2023,
Accepted 13th September 2023

DOI: 10.1039/d3cc02942e

rsc.li/chemcomm

Towards lithium-free solid-state batteries with nanoscale Ag/Cu sputtered bilayer electrodes†

Lorenzo Fallarino,^a Uzair Naveed Chishti,^a Arianna Pesce,^a Grazia Accardo,^a Amna Rafique,^{abc} Montserrat Casas-Cabanas^{ad} and Pedro López-Aranguren^{ib*}

Enhancing the reversible Li growth efficiency in “Li-free” solid-state batteries is key for the deployment of this technology. Here, we demonstrate a nanoscale material design path that enables the reversible cycling of a lithium-free solid-state battery, using Li₇La₃Zr₂O₁₂ (LLZO) electrolyte. By means of nanometric Ag–Cu bilayers, directly sputtered onto the LLZO, we can effectively control Li deposition. The robust thin film bilayer, which is compatible with LLZO, enables stable cycling, accommodating the volume changes without the need for extra external pressure.

Solid-state batteries (SSBs) show great promise in facilitating the widespread adoption of electric vehicles.^{1,2} Along with the replacement of flammable liquid electrolytes, which would lead to higher safety standards, SSBs may enable the use of lithium metal as anode, allowing for a dramatic increase in energy density, especially compared to standard graphite anodes.³ However, due to the high Li-reactivity, the assembly of pure Li–metal with solid-electrolytes (SEs) with a low SE–Li interfacial resistance remains a major challenge from both manufacturing and processing points of view.⁴

In this regard, the “Li-free” cell concept, in which the Li metal anode is *in situ* electroplated onto the current collector (CC), represents an opportunity to circumvent the aforesaid challenges.^{5,6} Moreover, it allows for minimizing the amount of required lithium, resulting in cost and sustainability improvements. In this context, LLZO is an appealing electrolyte to develop such a battery architecture, due to its high ionic conductivity and excellent stability against Li metal.⁷ In

addition, unlike thin-film batteries,⁶ limited to tens of $\mu\text{A cm}^{-2}$, bulk LLZO enables high-power and energy applications. However, recent studies investigating the Li nucleation behaviour at the SE/CC report that Li is plated with a non-uniform morphology, resulting in highly heterogeneous interfaces.^{8,9} This would inhibit the growth of lithium as a film-like anode, leading to unexpectedly premature short circuiting.^{8–10} Intriguingly, the lithium-growth characteristics can be significantly improved when the SE surface is modified by an artificial interlayer, such as AgC,¹¹ Ag,^{12–14} or Au.^{15–17} These materials alloy with lithium at a potential that is very close to that of the Li/Li⁺ redox reaction, thus suppressing the nucleation barriers.^{15,18} This is in contrast to the case of Si or Sn,^{19,20} which undergo major structural changes while alloying with lithium. As a result, the lithium deposition at the CC can potentially be effectively regulated, with the Ag or Au interlayer acting, during battery operation, as a sort of dynamic buffer layer for homogenous lithium redistribution.^{15,18}

Herein, we focus on the development of optimal artificial interfaces by sputtering a nanometric bilayer on top of an LLZO–SE, consisting of a 100 nm thick Ag dynamic buffer interlayer, and of a Cu layer, either 600 nm or 900 nm thick, which acts as a CC. Cu has been selected as the CC because of its high electrical conductivity and electro(chemical) stability against both Ag and Li.^{21,22} Directly sputtering onto the LLZO–SE is key to minimize the interfacial resistance that would ordinarily be unreachable for current collector foils. A schematic representation of the “Li-free” solid-state half-cell configuration, including its specific layer sequence and thicknesses, is shown in Fig. 1(a). The sputter deposition of Ag and Cu has been carried out at room temperature using a pressure of 4×10^{-1} Pa of pure Ar atmosphere without breaking the vacuum (base pressure lower than 1.2×10^{-5} Pa), to ensure high quality LLZO/Ag and Ag/Cu interfaces. Fig. 1(b) depicts the fabrication steps of the nanometric bilayer.

To investigate the formation of the Li–Ag alloy, we first assembled a Li/LLZO/Ag(100 nm)/Cu-foil half-cell. The Cu-foil was used to facilitate the post-mortem analysis by peeling it after the Li deposition. Fig. 2(a) shows the electrochemical

^a Centre for Cooperative Research on Alternative Energies (CIC energiGUNE), Basque Research and Technology Alliance (BRTA), Alava Technology Park, Albert Einstein 48, Vitoria-Gasteiz 01510, Spain. E-mail: plopez@cicenergigune.com

^b University of Basque Country (UPV/EHU), Barrio Sarriena, s/n, Leioa 48940, Spain

^c ALISTORE-European Research Institute, Hub de l'Energie, FR CNRS 3104, 15 rue Baudelocque, 80039 Amiens, France

^d Ikerbasque, The Basque Foundation for Science, Plaza Euskadi 5, Bilbao 48009, Spain

† Electronic supplementary information (ESI) available. See DOI: <https://doi.org/10.1039/d3cc02942e>



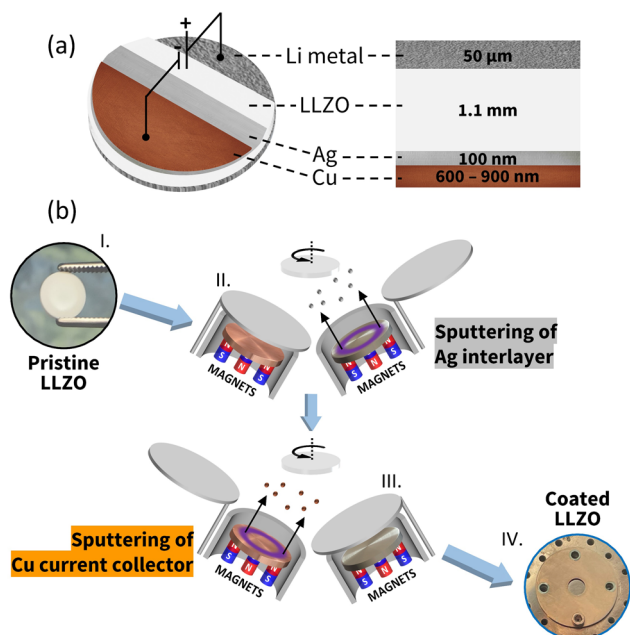


Fig. 1 (a) Half-cell schematic. (b) Fabrication steps of the bilayer: (I) photo of the pristine LLZO; (II) Ag interlayer sputtering process; (III) subsequent Cu sputtering step; (IV) photo of the coated LLZO pellet by the Ag–Cu bilayer, with the characteristic Cu colour. The mask is also visible, which has been used to avoid coating the pellet sides.

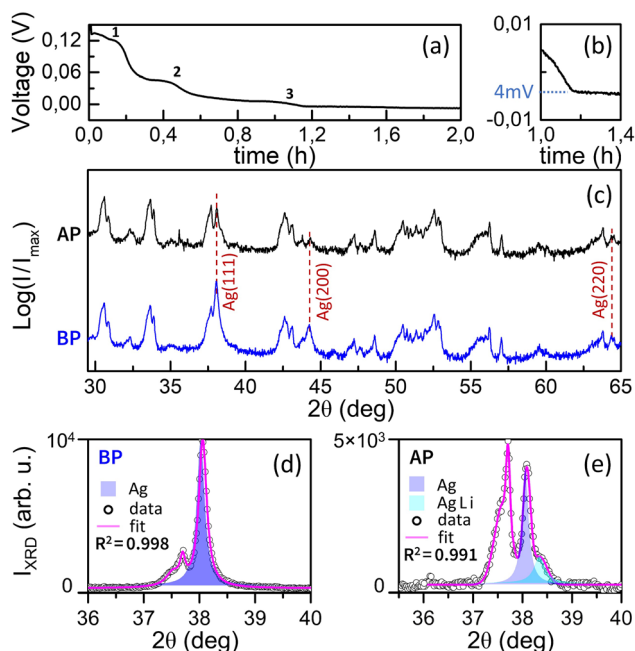


Fig. 2 (a) Voltage profiles of Li electroplating at $j = 0.05 \text{ mA cm}^{-2}$ of a Li/LLZO/Ag(100 nm)/Cu-foil cell at $T = 70^\circ\text{C}$. The numbers 1, 2, and 3 indicate the alloying-steps. (b) Zoomed in view of (a); (c) XRD $\theta/2\theta$ scan for the same cell before (blue, BP) and after (black, AP) Li-plating. (d) and (e) Data analysis of the XRD data around the Ag (111) peak position.

response measured at $T = 70^\circ\text{C}$ under a current density of $j = 0.05 \text{ mA cm}^{-2}$. Li metal directly plating onto bare Cu typically

exhibits a sudden voltage drop at the beginning of Li metal deposition, which is ascribed to the nucleation potential, and is followed by a flat voltage plateau corresponding to the Li growth step.^{9,16,23} Due to the large Li/Cu thermodynamic mismatch, a meaningful overpotential is necessary to overcome the heterogeneous nucleation barriers onto Cu.^{16,24} In contrast, as shown in Fig. 2(a), the process exhibits three clear voltage steps at positive values ($V_1 \approx 7 \text{ mV}$, $V_2 \approx 45 \text{ mV}$, and $V_3 \approx 120 \text{ mV}$), similar to the case of Au interlayers,¹⁵ suggesting the alloying of Li with Ag.¹⁵ Afterwards, the Li metal deposition potential does not show any voltage dip, as for pure Cu, but only a smooth turn towards the voltage onset (Fig. 2b). The Li metal nucleation overpotential through the Li–Ag interlayer onto the Cu foil is found to be as low as $V_{\text{OP}} \approx 4 \text{ mV}$.

To characterize the Li–Ag alloy and the LLZO integrity at the end of the full alloying process, structural analysis before plating (BP) and after plating (AP) was performed by X-ray diffraction (XRD) $\theta/2\theta$ scans with Cu- K_α radiation (Fig. 2(c)). Both scans look nearly identical in their overall appearance, exhibiting well-defined diffraction peaks corresponding to both cubic and tetragonal structured LLZO electrolyte (as detailed along with Fig. S1, ESI†) and Ag interlayer, the latter highlighted by (red) dashed lines. However, after the Li-plating step, while the diffraction peaks corresponding to the LLZO remain unchanged, confirming the structural stability of the electrolyte after operating under high temperature (as detailed along with Fig. S2, ESI†), those corresponding to the Ag interlayer exhibit significant differences. The intensity of all three peaks decreases substantially. Moreover, a shoulder is clearly visible at the right of the Ag (111) peak. Fig. 2(d) and (e) display the least-squares fit as a (pink) solid line, by using a multi-Lorentzian fitting function, in direct comparison with the data around the Ag (111) diffraction peak position. In each case, we find excellent agreement between the experimental data and the least-squares fit, with $R^2 > 0.99$. The extracted Ag (111) diffraction angle for the BP case corresponds to $2\theta = 38.04^\circ \pm 0.01^\circ$, in very good agreement with bulk values and reported data.²⁵ On the contrary, in the case of AP, the occurrence of a second diffraction peak at a higher angle is clearly visible, which, according to the electrochemical response of Fig. 2(a), we ascribe to an Ag_xLi_y alloy. The extracted angular position of both peaks is $2\theta_{\text{Ag}} = 38.08^\circ \pm 0.02^\circ$ and $2\theta_{\text{Ag}_x\text{Li}_y} = 38.41^\circ \pm 0.02^\circ$. To determine the alloy composition, we have evaluated the lattice spacing corresponding to the Ag_xLi_y diffraction angle, as detailed in the supplementary materials, and compared it to previous works.^{26–29} As a result, Ag_xLi_y should correspond to $\text{Ag}_{46\pm4}\text{Li}_{54\pm4}$, in agreement with the fact that intermetallic compounds with a Ag:Li ratio close to 1:1 exhibit the lowest formation enthalpy.^{26–29} However, a residual amount of Ag seems to not be alloying with lithium, due to the presence of very low intensity (not angular shifted) Ag (200) and Ag (220) diffraction peaks after the Li-plating step. This suggests that Ag and Li do not form a purely solid solution as expected, but, instead, a two-phase reaction occurs.¹⁴ It is worth highlighting that, as expected for a 2-phase reaction, the intensity of the Ag peaks decreases as the new phase Ag–Li forms.



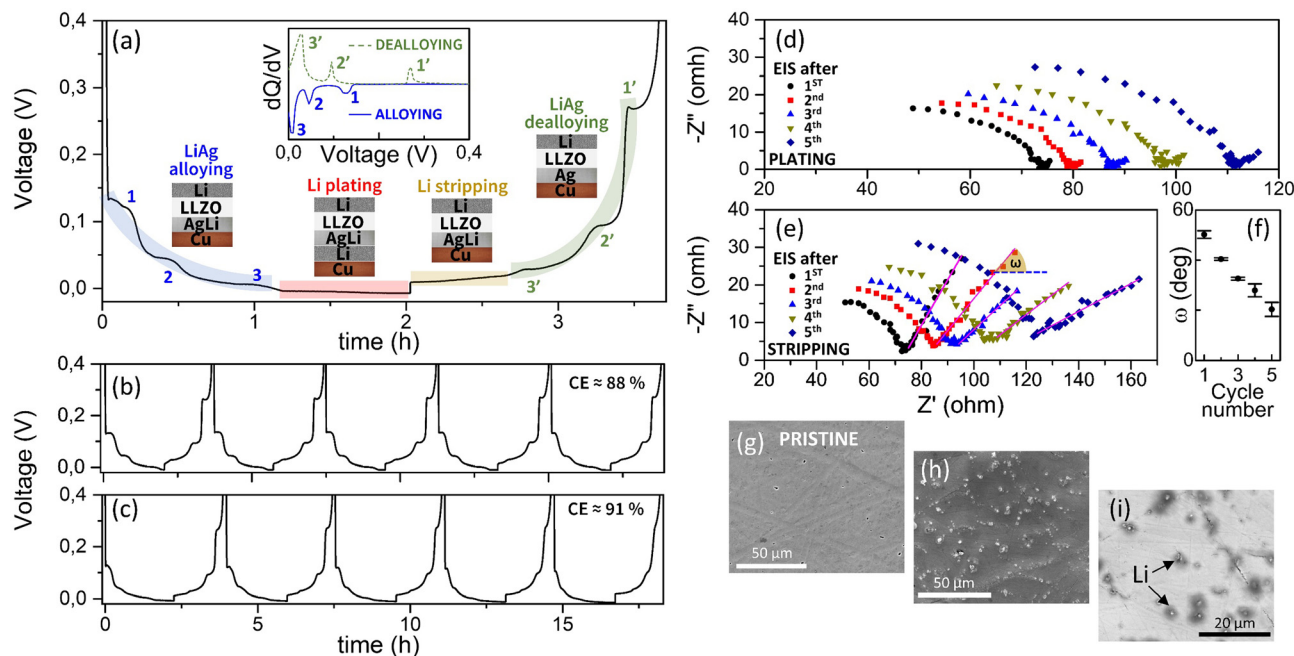


Fig. 3 (a) Initial potential response of Li/LLZO/Ag(100 nm)/Cu(600 nm) after plating/stripping at $j = 0.05 \text{ mA cm}^{-2}$ and at $T = 70^\circ\text{C}$. The schematics show the layer structure evolution upon cycling; the inset shows the differential capacity as a function of the cell voltage. Voltage profile of (b) Li/LLZO/Ag(100 nm)/Cu(900 nm) and (c) Li/LLZO/Ag(100 nm)/Cu(600 nm) at $j = 0.05 \text{ mA cm}^{-2}$ and at $T = 70^\circ\text{C}$. Impedance spectra of Li/LLZO/Ag(100 nm)/Cu(600 nm) after plating (d) and stripping (e) steps at a current density $j = 0.05 \text{ mA cm}^{-2}$ at $T = 70^\circ\text{C}$. (f) Warburg angle ω as a function of cycle number. (g) SEM images of the Cu surface before any electrochemical testing. *Ex situ* SEM (h) and BSE (i) of the Cu surface after 5 plating/stripping cycles at $j = 0.05 \text{ mA cm}^{-2}$ plus 5 plating/stripping cycles at $j = 0.10 \text{ mA cm}^{-2}$.

The reversibility of the Li plating through the Ag_xLi_y layer onto a thin sputtered Cu CC was investigated by continuous plating/stripping processes. Fig. 3(a) shows the whole cycling profile of the Li/LLZO/Ag(100 nm)/Cu(600 nm) cell. Three “discharge” voltage steps are clearly distinguishable at $V \approx 7 \text{ mV}$, 45 mV , and 120 mV , highlighted in (light) blue, followed by the Li plating at $V < 0 \text{ V}$. By taking into account the theoretical conversion of a 1 mA h cm^{-2} to $5 \mu\text{m}$ thick Li layer,³⁰ as explained in detail in the supplementary materials, the evolution of the corresponding alloy stoichiometries (and errors) may also be calculated. This would lead to the alloying sequence of $\text{Ag} \rightarrow (1) \text{Ag}_{86 \pm 2}\text{Li}_{14 \pm 2} \rightarrow (2) \text{Ag}_{58 \pm 6}\text{Li}_{42 \pm 6} \rightarrow (3) \text{Ag}_{37 \pm 6}\text{Li}_{63 \pm 6}$, with the latest value being different with respect to the one calculated by the XRD peak position. However, due to the inherent error of the Li quantity conversion that assumes a perfect process, which may not occur in the reality, such values could overestimate the Li quantity in the alloys and be less accurate than the ones extracted from the X-ray measurements.

Besides, the reversibility of the process is confirmed by the similar plateaus observed at $V \approx 27 \text{ mV}$, 95 mV , and 270 mV , highlighted in light green, corresponding to the dealloying reaction sequence. In between, the plateaus related to the plating and stripping of Li onto the Cu CC are visible and highlighted in red (plating) and yellow (stripping). The inset in Fig. 3(a) displays the differential capacity as a function of the cell voltage, for the alloying process in (blue) solid line and for the dealloying process in (green) short dashed line. Three well

defined peaks for each galvanostatic process are visible, named 1 (1'), 2 (2'), and 3 (3'). Their positions along the x-axis, related to the same process, exhibit different voltage shifts, which indicates a stronger cell polarization for the $\text{Ag} \rightarrow (1) \text{Ag}_{86 \pm 2}\text{Li}_{14 \pm 2}$ reaction. This suggests that, by having an Ag_xLi_y alloy as the starting interlayer, the cell polarization may be fairly reduced, since the Ag-rich (de-)alloying processes would be avoided, as long as the corresponding reaction voltage would not be accessed while cycling.¹³

The full cycling of the half-cells with Cu (900 nm) and Cu (600 nm), upon applying the same cycling parameters as in Fig. 3(a) are displayed in Fig. 3(b) and (c), respectively. In both cases, the voltage profile is similar upon increasing the number of plating/stripping processes irrespective of the Cu thickness. This would further demonstrate that the three plating/stripping steps are ascribable to the Ag–Li (de-)alloy formation. The promising Coulombic efficiency (CE), obtained from the full process (alloying and plating) and averaged over the first 5 cycles, is above 88% for both cells, confirming the viability of our nanoscale anode material design pathway. The slight differences in the voltage profile and CE are likely due to the differences in the surface roughness and ionic conductivity from pellet to pellet.⁷ However, here, the CE does not pretend to point to a battery performance improvement, for which a far longer cycle performance study would be needed.

Galvanostatic electrochemical impedance spectroscopy (GEIS) was carried out to gain further insight into the evolution of the interfacial resistance and the Ag interlayer during the



consecutive plating/stripping processes. The corresponding Nyquist plots are shown in Fig. 3(d), after each plating step, and in Fig. 3(e), after the subsequent stripping processes. The spectra in Fig. 3(d) are characterized by a semicircle at high frequency, ascribed to the interfacial resistance between the Li electrode and the LLZO electrolyte, which is partially measured due to the frequency range selected for this experiment (10 kHz to 1 Hz). This resistance seems to slightly increase at each plating step. More importantly, at low frequencies, the capacitive behaviour of the blocking CC to Li^+ is barely visible, since, after Ag_xLi_y alloy formation, and after Li deposition onto the Cu, the anodic part of the cell converts into a charge transfer component, due to the non-blocking nature of Li. On the contrary, after each stripping step, the impedance spectra exhibit solely capacitive behaviour at low frequencies due to the recovered blocking nature of the CC, suggesting the potential complete de-alloying process of Ag_xLi_y . The characteristic Warburg diffusion element, represented by the tail appearing at low frequency, should show a phase angle $\omega = 45^\circ$. However, as shown in Fig. 3(f), ω decreases upon increasing the number of plating/stripping cycles, which may indicate a chemical or structural evolution of the Ag/Cu bilayer upon alloying/dealloying consecutive processes. Moreover, an increase in resistance is also visible, as in the plating case, which can be due to the contact loss at the LLZO/Ag interface.

SEM micrographs performed after GEIS are reported in Fig. 3(h) and (i), together with the pristine sample in Fig. 3(g). The SEM micrographs reveal that the addition of the Ag layer prevents the Cu-CC from breaking during stripping/plating.^{8,17,31} In fact, due to alloying of Li and Ag, nucleation of Li onto Cu may then be more homogeneous because the AgLi layer acts as a seed layer for Li nucleation.

In this study, we have investigated the effect of Ag–Cu bilayer nanomaterials on the electrochemical lithium deposition. We found that the lithium nucleation and growth behaviour is significantly altered by the LLZO surface modification thanks to the artificial interlayer, and that lithium distribution on the Cu-CC can be effectively controlled. Considering the convenience of interlayer sputter deposition on the LLZO surface and its wide applicability, we expect that our findings will provide useful guidelines for designing optimal interfaces for solid state batteries, especially enabling a “Li-free” sample architecture. Moreover, this work poses the basis for more applied and consecutive ones, that might focus on long cycle performance of the half and full cell. Finally, given the generality of the Li–Ag alloy formation, we expect that our findings will extend to many different garnet electrolyte materials and metallic current collectors.

This work was supported by the “MCIN/AEI”, under the project grant TED2021-129663B-C52 and is part of R&D&I projects PLEC2022-009412 (MCIN/AEI/10.13039/501100011033) and by “ERDF A way of making Europe”, by the “European Union” and by the “EU NextGenerationEU/PRTR”. As a part of the DESTINY PhD programme, this publication received funding from the EU's Horizon2020 research and innovation programme under the

Marie Skłodowska Curie Actions COFUND (Grant Agreement #945357).

Conflicts of interest

There are no conflicts to declare.

Notes and references

- 1 J. Janek and W. G. Zeier, *Nat. Energy*, 2016, **1**, 1–4.
- 2 S. Randau, D. A. Weber, O. Kötter, R. Koerver, P. Braun, A. Weber, E. Ivers-Tiffée, T. Adermann, J. Kulisch, W. G. Zeier, F. H. Richter and J. Janek, *Nat. Energy*, 2020, **5**, 259–270.
- 3 B. Acebedo, M. C. Morant-Miñana, E. Gonzalo, I. Ruiz de Larra-mendi, A. Villaverde, J. Rikarte and L. Fallarino, *Adv. Energy Mater.*, 2023, **13**, 2203744.
- 4 A. Sharafi, E. Kazyak, A. L. Davis, S. Yu, T. Thompson, D. J. Siegel, N. P. Dasgupta and J. Sakamoto, *Chem. Mater.*, 2017, **29**, 7961–7968.
- 5 J. Qian, B. D. Adams, J. Zheng, W. Xu, W. A. Henderson, J. Wang, M. E. Bowden, S. Xu, J. Hu and J.-G. Zhang, *Adv. Funct. Mater.*, 2016, **26**, 7094–7102.
- 6 B. J. Neudecker, N. J. Dudney and J. B. Bates, *J. Electrochem. Soc.*, 2000, **147**, 517.
- 7 H. Sun, S. Kang and L. Cui, *Chem. Eng. J.*, 2023, **454**, 140375.
- 8 T. Fuchs, J. Becker, C. G. Haslam, C. Lerch, J. Sakamoto, F. H. Richter and J. Janek, *Adv. Energy Mater.*, 2023, **13**, 2203174.
- 9 M. J. Wang, E. Carmona, A. Gupta, P. Albertus and J. Sakamoto, *Nat. Commun.*, 2020, **11**, 5201.
- 10 K. Lee, E. Kazyak, M. J. Wang, N. P. Dasgupta and J. Sakamoto, *Joule*, 2022, **6**, 2547–2565.
- 11 J.-S. Kim, G. Yoon, S. Kim, S. Sugata, N. Yashiro, S. Suzuki, M.-J. Lee, R. Kim, M. Badding, Z. Song, J. Chang and D. Im, *Nat. Commun.*, 2023, **14**, 782.
- 12 T. Liu, Q. Hu, X. Li, L. Tan, G. Yan, Z. Wang, H. Guo, Y. Liu, Y. Wu and J. Wang, *J. Mater. Chem. A*, 2019, **7**, 20911–20918.
- 13 S. Jin, Y. Ye, Y. Niu, Y. Xu, H. Jin, J. Wang, Z. Sun, A. Cao, X. Wu, Y. Luo, H. Ji and L.-J. Wan, *J. Am. Chem. Soc.*, 2020, **142**, 8818–8826.
- 14 H. J. Choi, D. W. Kang, J.-W. Park, J.-H. Park, Y.-J. Lee, Y.-C. Ha, S.-M. Lee, S. Y. Yoon and B. G. Kim, *Adv. Sci.*, 2022, **9**, 2103826.
- 15 S. Kim, C. Jung, H. Kim, K. E. Thomas-Alyea, G. Yoon, B. Kim, M. E. Badding, Z. Song, J. Chang, J. Kim, D. Im and K. Kang, *Adv. Energy Mater.*, 2020, **10**, 1903993.
- 16 K. Yan, Z. Lu, H.-W. Lee, F. Xiong, P.-C. Hsu, Y. Li, J. Zhao, S. Chu and Y. Cui, *Nat. Energy*, 2016, **1**, 16010.
- 17 T. Krauskopf, R. Dippel, H. Hartmann, K. Peppler, B. Mogwitz, F. H. Richter, W. G. Zeier and J. Janek, *Joule*, 2019, **3**, 2030–2049.
- 18 X. Liang, Q. Pang, I. R. Kochetkov, M. S. Sempere, H. Huang, X. Sun and L. F. Nazar, *Nat. Energy*, 2017, **2**, 1–7.
- 19 P. Zheng, J. Sun, H. Liu, R. Wang, C. Liu, Y. Zhao, J. Li, Y. Zheng and X. Rui, *Batteries Supercaps*, 2023, **6**, e202200481.
- 20 P. Nithyadharani, M. V. Reddy, B. Nalini, M. Kalpana and B. V. R. Chowdari, *Electrochim. Acta*, 2015, **161**, 261–268.
- 21 I. T. Roe and S. K. Schnell, *J. Mater. Chem. A*, 2021, **9**, 11042–11048.
- 22 Z. Xiong, S. Shi, C. Ouyang, M. Lei, L. Hu, Y. Ji, Z. Wang and L. Chen, *Phys. Lett. A*, 2005, **337**, 247–255.
- 23 B. Thirumalraj, T. T. Hagos, C.-J. Huang, M. A. Teshager, J.-H. Cheng, W.-N. Su and B.-J. Hwang, *J. Am. Chem. Soc.*, 2019, **141**, 18612–18623.
- 24 S. F. Liu, X. L. Wang, D. Xie, X. H. Xia, C. D. Gu, J. B. Wu and J. P. Tu, *J. Alloys Compd.*, 2018, **730**, 135–149.
- 25 L. Fallarino, O. Hovorka and A. Berger, *Phys. Rev. B*, 2016, **94**, 064408.
- 26 A. Dębski, S. Terlicka, A. Budziak and W. Gąsior, *J. Alloys Compd.*, 2018, **732**, 210–217.
- 27 M. H. Braga, A. Dębski, S. Terlicka, W. Gąsior and A. Góral, *J. Alloys Compd.*, 2020, **817**, 152811.
- 28 V. V. Pavlyuk, G. S. Dmytriv, I. I. Tarasiuk, I. V. Chumak, H. Pauly and H. Ehrenberg, *Solid State Sci.*, 2010, **12**, 274–280.
- 29 A. D. Pelton, *Bull. Alloy Phase Diagrams*, 1986, **7**, 223.
- 30 S. Chen, C. Niu, H. Lee, Q. Li, L. Yu, W. Xu, J.-G. Zhang, E. J. Dufek, M. S. Whittingham, S. Meng, J. Xiao and J. Liu, *Joule*, 2019, **3**, 1094–1105.
- 31 M. Motoyama, M. Ejiri and Y. Iriyama, *J. Electrochem. Soc.*, 2015, **162**, A7067–A7071.

